



Fracture propagation and permeability evolution mechanism of jointed rock mass in coastal mines

Bingqian Yan^{1,2,3} · Qingjie Qi^{1,2,3} · Jianzhong Liu^{2,3} · Meifeng Cai⁴ · Xiangshang Li^{2,3} · Peitao Wang⁴

Received: 17 May 2022 / Accepted: 8 December 2022 / Published online: 19 December 2022
© The Author(s), under exclusive licence to Springer-Verlag GmbH Austria, part of Springer Nature 2022

Abstract

To study the fracture propagation mechanism and the permeability evolution of the fault fracture zone in coastal deep mines, the nuclear magnetic resonance (NMR) tests and the triaxial mechanical properties tests of rock specimens rock mass specimens with different joint dip angles under hydro-mechanical coupling were carried out. Based on the investigation of the surrounding rock joints and the analysis of rock composition, the rock physics experimental model was prepared. The evolution mechanism of rock porosity is obtained by NMR test. The changes of mechanical properties, acoustic emission (AE) and permeability characteristics of rock specimens with different joint dip angles were studied, and the evolution mechanism of permeability properties with different joint dip angles is revealed by combining the microstructure and joint tip expansion mechanism. When the jointed rock mass specimens reach the peak stress, the bearing capacity of the specimens decreases slowly, and the specimens show the characteristics of progressive failure. The specimen generates micro-cracks at the joint tip under the action of axial pressure, micro-cracks evolve and expand with the increase of pressure, the permeability coefficient gradually increases. The main fracture of jointed rock mass specimens is the fracture that originates from the joint tip and extends along the axial direction until the specimen loses its bearing capacity.

Highlights

- Evolution mechanism of permeability properties was revealed.
- The microstructure and joint tip expansion mechanism were studied.
- The fracture propagation law of jointed rock mass specimens was investigated.

Keywords NMR · Fracture propagation · Acoustic emission · Permeability coefficient · Microstructure

✉ Xiangshang Li
xiangshang_li@126.com

¹ China Coal Research Institute, Emergency Science Research Institute, Beijing 100013, China
² China Coal Technology and Engineering Group, China Coal Research Institute, Beijing 100013, China
³ State Key Laboratory of Coal Mining and Clean Utilization, China Coal Technology and Engineering Group, Beijing 100013, China
⁴ School of Civil and Resource Engineering, University of Science and Technology Beijing, Beijing 100083, China

1 Introduction

Water inrush in mine roadway is one of the main threats affecting mining production. In underwater mining, the mining of fault rock mass is especially faced with the threat of surrounding rock instability and water inrush (Wu et al. 2016). The analysis of water-filled factors and water-conducting fracture zone of surrounding rock in the process of mining is not only an important link to prevent mine accidents such as mine water inrush (Ardeshir et al. 2014), but also the main index to evaluate mine water drainage design and determine mine production capacity (Wolkersdorfer et al. 2020). The occurrence environment of the Sanshan-dao Gold Mine belongs to a typical gold mine with altered

rock in fault fracture zone (Vaziri et al. 2018). After half a century of large-scale mining (Małachowski et al. 2018), the exploration and mining depth has reached an elevation of more than 1 km (Wang et al. 2020). The hydrogeological conditions in the mining area have changed to some extent (Polak et al. 2016). In the process of mining, the pit water inflow shows an increasing trend year by year (Cui et al. 2019), which has a certain impact on mine safety production (Xue et al. 2020). Therefore, exploring the current hydrogeological conditions in the mining area (Shi et al. 2019), analyzing the factors of water filling in the mining area, and studying the penetration mechanism and water-conducting channels of surrounding rock fractures are the basis for formulating the water inrush prevention scheme (Song et al. 2021), which has important guiding significance for ensuring the safe and efficient mining of deep mineral resources (Li et al. 2017).

At present, many countries in the world have entered the stage of mining mineral resources to a depth of more than 1000 m (Liu et al. 2012). Deep mining operation must address two major challenges: (a) efficient excavation; and (b) control of mining-induced catastrophic rock instabilities and dangerous fluid inrush (Wang et al. 2016 and 2019). The mine water inrush accidents encountered in deep mining will threaten the safety of many workers every year, especially mines mining ore bodies under the seabed and water bodies (Hassani et al. 2018). The engineering and research of underwater mineral resources mining in China started relatively late (LaMoreaux et al. 2014), but it has also made great development in recent years (Lee et al. 2021). Through the research on the influencing factors of water inrush in the surrounding rock of the mine (Cai 2016), scholars have made great progress in the hydraulic model of water inrush (Golian et al. 2018), fluid seepage, failure of surrounding rock, and the change of mining dynamic stress (Khave et al. 2014), which has played a positive role in studying the mechanism and prevention of water inrush in the roof and floor of the mine (Wu et al. 2019). The mining of ore bodies under sea, rivers, reservoirs, and lakes in China has also obtained experience that is worthy of reference for other underwater mines (Wang et al. 2017). However, due to the existence of mine surrounding rock joints, there are some differences in their anisotropic characteristics and failure mechanism (Li et al. 2016). Further work is required to study the evolution process of rock fracture propagation and permeability (Zhou et al. 2018).

Through the test of rocks with different lithology (Pappalardo. 2018), it is concluded that the hydraulic conductivity and stress have negative exponent. The seepage test of granite is carried out (Ren et al. 2020), and the calculation formula of power function between permeability coefficient and stress is obtained. Zhang et al. (2013) studied

the compression failure of granite under different seepage pressures and confining pressures, and found that the peak strength reduction coefficient increases linearly with the increase of pore pressure, and the change rate decreases with the increase of confining pressure. They also pointed out that the dilatancy of rock volume and water rock coupling are mutually reinforcing. Yu et al. (2015) also found that confining pressure and seepage pressure have opposite effects on the strength of rock, and the increase of seepage pressure will promote the reduction of rock strength and crack growth. The above analysis shows that the mechanical properties of rock under hydro-mechanical coupling are obviously deteriorated, and the application of seepage pressure promotes the crack growth of rock. It is believed that the influence of water solution on the internal microstructure of rock is the internal cause of rock macro mechanical damage (Gao et al. 2018). However, due to the limitation of test technology, it is impossible to have a clear understanding of the development process of rock surface cracks under water rock coupling.

In underground mining, the catastrophic damage of the surrounding rock of the mine will lead to the sudden groundwater influx accidents on the mining face and heading face (Yan et al. 2020a, b), which will pose a great security threat to the mine staff and mining equipment (Ma et al. 2017). For underwater mines, mine water inrush not only seriously threatens the life safety of personnel (Yao et al. 2012), but also greatly restricts the productivity of mines (Zhang et al. 2009). Therefore, the evolution mechanism of mechanical properties and permeability of the surrounding rock in the mine (Yan et al. 2020a, b) needs to be further studied to further analyze the physical and mechanical characteristics of rock mass with different joint dip angles and the expansion law of joint cracks, providing theoretical support for the stability of mine surrounding rock and the prevention of water inrush.

2 Investigation of surrounding rock and NMR test of rock specimens

2.1 Investigation and statistical analysis of surrounding rock joints

Sanshandao Gold Mine is the first metal mine in China to mine under sea. The deep rock mass contains a fracture zone and fault structure. Due to the existence of joints and the influence of some altered interlayer, the strength of the rock mass is reduced (Castro et al. 2007). The total length of joint survey line is 80 m, and a total of 169 joints (micro-fissures were omitted during measurement), with joint spacing ranging from 0.1 to 10.8 m. According to the pole map, the poles

of joints are scattered around a center within a certain range, which is the dominant occurrence of joints. According to the method of dividing the dominant occurrence of joints, a software for interactive analysis based on geological data azimuth (DIPS software) developed by M.S. Diederichs and E. Hoek is used to make joint rose map and pole isodensity map, and interactive analysis is carried out on the basis of joint geological azimuth data statistics.

2.1.1 1 Joint rose diagram method

Inclination: 18 intervals are divided every 10°, and the number of joints r_i ($i = 1, 2, \dots, 18$) in each interval and the arithmetic mean value z_i ($i = 1, 2, \dots, 18$) of inclination in each interval are counted.

Strike: 18 intervals are divided every 10° (subtract 180° if the strike angle is greater than 180°), and the number of joints r_i ($i = 1, 2, \dots, 18$) in each interval and the arithmetic mean value z_i ($i = 1, 2, \dots, 18$) of inclination in each interval are counted.

The coordinates (x_i, y_i) of each section are obtained as follows:

$$\begin{cases} x_i = \frac{r_i}{R} \times R_{100} \times \sin z_i \\ y_i = \frac{r_i}{R} \times R_{100} \times \cos z_i \end{cases} \quad (1)$$

where: R_{100} —circle radius, taken as 100; r_i ($i = 1, 2, \dots, 18$)—number of joints in each interval; R —the maximum number of joints in 18 intervals.

2.1.2 2 Schmidt's equal-area method

When using Schmidt projection network to divide the dominant occurrence of joints, first convert the occurrence data of structural plane into (x, y) coordinates of rectangular coordinate system, and the normal of structural plane is projected to the upper hemisphere. The relationship is as follows:

When using the Schmidt projection network to divide the joint dominant occurrences, the structural surface occurrence data is first converted to the (x, y) coordinates of the Rectangular Coordinate System, and the structural plane normal is projected upwards in the hemisphere. The relationship is as follows:

$$O_p = 2r \times \sin \frac{\theta}{2} \quad (2)$$

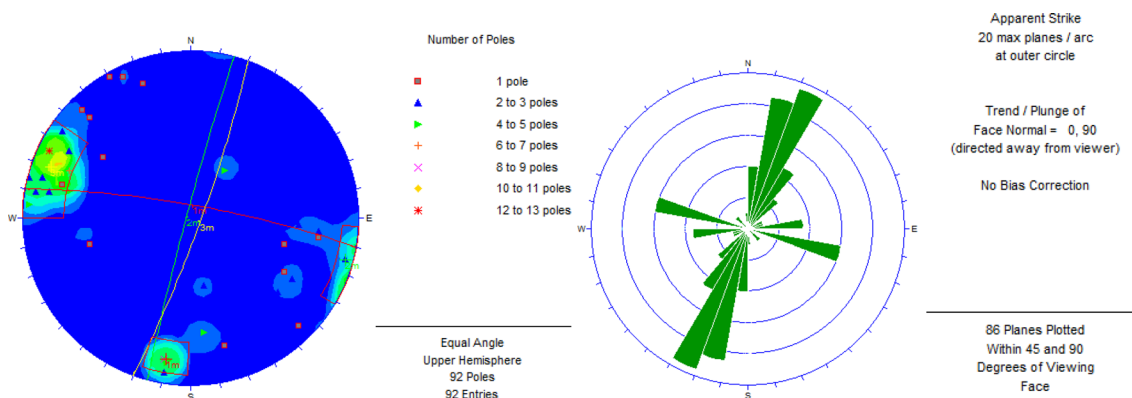
When inclination θ is 90°, $O_p = \sqrt{2}r \cdot S$, the distance d from the pole to the center of the circle is:

$$d = \frac{O_p}{\sqrt{2}} = \sqrt{2}r \times \sin \frac{\theta}{2} \quad (3)$$

Therefore, the pole coordinates after the normal projection of the structural plane can be obtained:

$$\begin{cases} x = \sqrt{2}r \times \sin \frac{\theta}{2} \times \sin \varphi \\ y = \sqrt{2}r \times \sin \frac{\theta}{2} \times \cos \varphi \end{cases} \quad (4)$$

The occurrence information of structural plane can also be deduced through pole coordinates:



(a) Pole map and contour cloud map of joint tendency (b) Rose map of joint strike

Fig. 1 Joint occurrence information (a) Pole map and contour cloud map of joint tendency (b) Rose map of joint strike

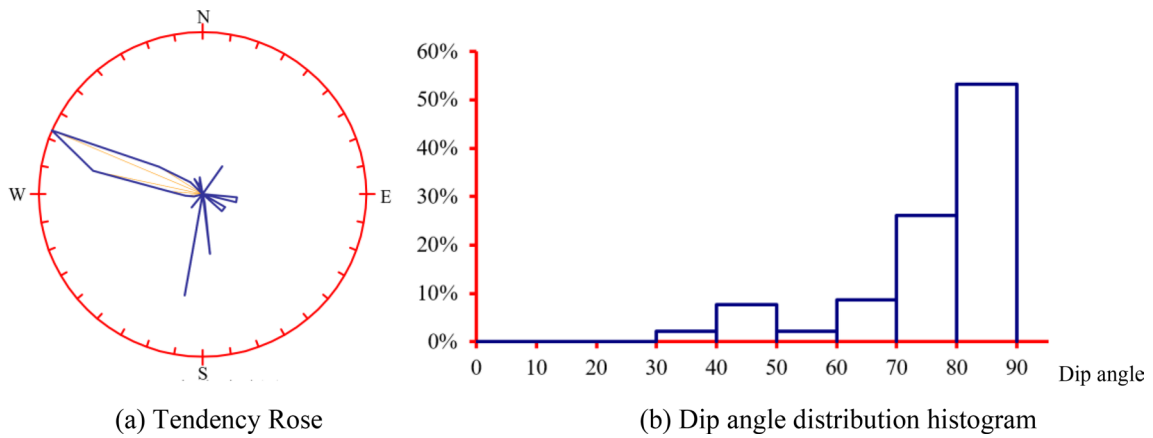


Fig. 2 Joint occurrence of surrounding rock Dip angle (a) Tendency Rose, (b) Dip angle distribution histogram

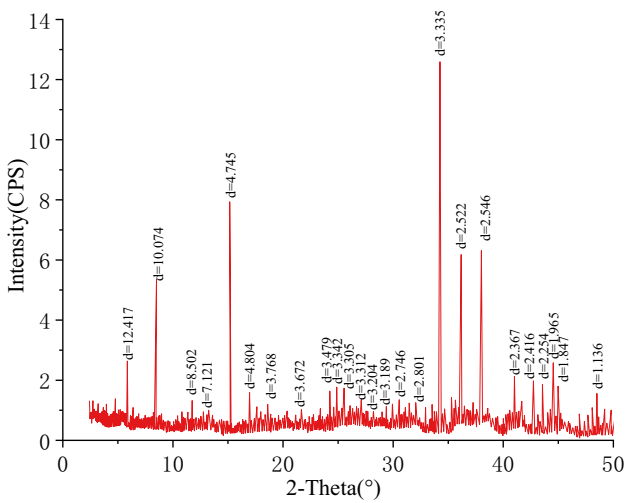


Fig. 3 X-ray diffraction pattern of granite specimen

$$\begin{cases} \theta = \arctg \frac{x}{y} \\ \varphi = 2 \arcsin \frac{x^2 + y^2}{2r^2} \end{cases} \quad (5)$$

where: φ —Tendency; θ —Dip angle.

After calculation according to the above formulas, the joint occurrence data is analyzed by DIPS software to draw the joint contour cloud map, pole map and joint strike rose map within the survey area, as shown in Fig. 1.

The rock mass in the middle section of—915 in Xishan mining area of Sanshandao Gold Mine is relatively broken, and the excavation exposure area is small. The measured rose diagram of joint fissure occurrence is shown in Fig. 2. Combined with the joint occurrence diagram completed with DIPS software (as shown in Fig. 1). The dominant direction of joints is roughly divided into three groups according to the tendency: the average inclination of the first group is 115.84° , and the average dip angle is 74.85° ; the average inclination of the second group was 184.74° , and the average dip angle was 67.35° ; the average inclination of the third group was 293.57° , and the average dip angle was 84.91° ; the dominant orientation can be roughly divided into two groups according to the strike: 190° and 295° , and the dip angle is mostly distributed at $40^\circ \sim 90^\circ$.

2.2 Parameter test of rock specimens

The rock used in the test is granite, and the selected granite material has few joints and good integrity. Through

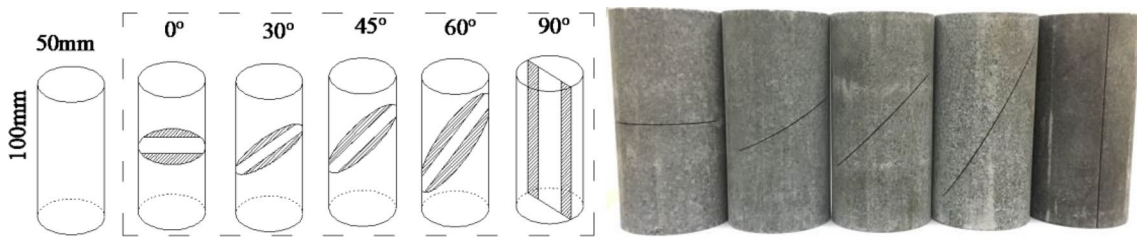


Fig. 4 Non-penetrating jointed rock mass specimens with different dip angles

the mineral composition analysis of granite specimen by X-ray diffraction (as shown in the Fig. 3), it is obtained that the main minerals of granite are quartz (25.8%), feldspar (37.6%), calcite (9.4%), dolomite (12.8%), montmorillonite (2.4%), illite (8.2%) and chlorite (3.8%).

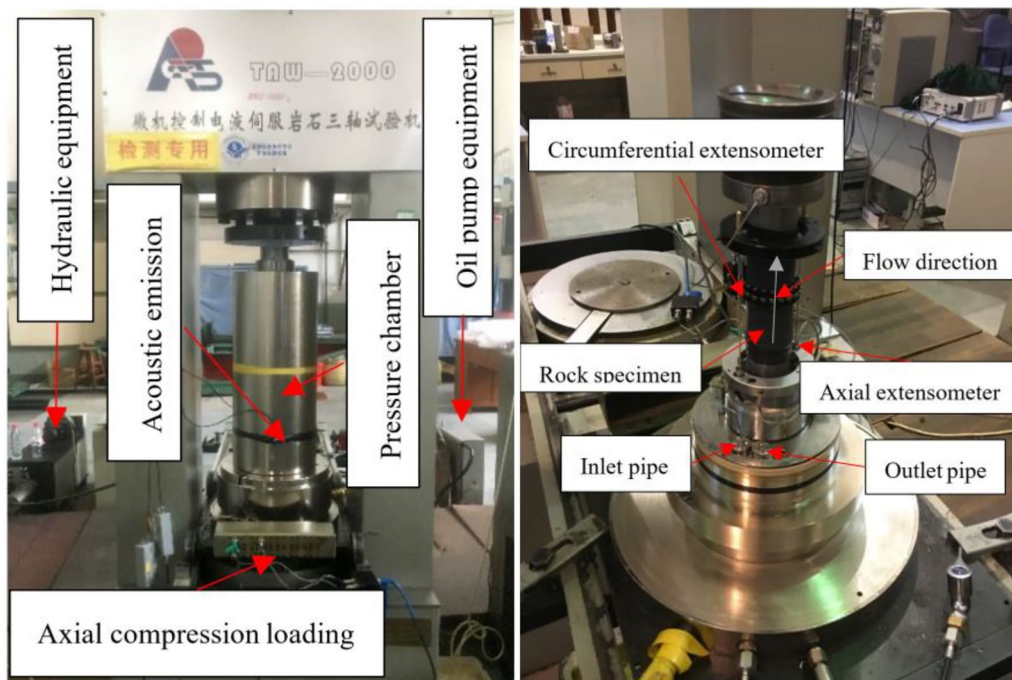
In the experiment, the jointed rock mass specimen is cut by artificial joints based on the drilled granite cylindrical rock specimen. To reduce the test error caused by the specimen itself, the same batch of rocks are selected for the test, the longitudinal wave velocity and density of rock specimens are tested, and the specimens with similar test results are selected for the joint processing and later test. The mineral composition of the granite specimen is shown in Fig. 3. The main size of the test specimens used in the test is a cylinder with a diameter of 50 mm and a height of 100 mm. The test specimens used in each working condition are three identical specimens.

The joint inclination angle was mainly considered in the preparation process of the specimen, and the joint inclination angles of the produced rock specimens were 0°, 30°, 45°, 60°, and 90° respectively (as shown in Fig. 4).

To study the deformation failure law and strength characteristics of rock mass specimens under triaxial compression, triaxial tests are mainly used. According to the stress state of the specimens in the test process, they can be divided into conventional triaxial tests (the stress state is $\sigma_1 > \sigma_2 = \sigma_3 > 0$)

and true triaxial test (stress state is $\sigma_1 > \sigma_2 > \sigma_3 > 0$). The conventional triaxial test is adopted in this paper. The experimental equipment is TAW-2000 microcomputer-controlled electro-hydraulic servo rock triaxial test equipment as shown in Fig. 5, including axial loading equipment, confining pressure equipment through oil pump, hydraulic seepage equipment and triaxial loading pressure chamber.

To prevent oil from entering the test specimen during confining pressure loading, the fixed test specimen shall be covered with heat shrinkable pipe and both ends of the heat shrinkable pipe shall be closed with electrical tape before the test, and then the axial extensometer and circumferential extensometer shall be installed. As shown in Fig. 5 (b), the test specimen shall be put into the pressure chamber, and the water flow shall be tested to see if it is normal. The water inlet pipe, drainage pipe and extensometer data collector shall be installed. After the test specimen is installed, the pressure chamber is sleeved with the confining pressure cylinder and filled with oil, and the cylinder is slowly lifted to make the top of the pressure chamber close to the loading device. Acoustic emission technology is also used in the test, and the acoustic emission equipment is arranged on the outer wall of the pressure chamber.



(a) Triaxial test equipment (b) Axial, circumferential and hydraulic measurement system

Fig. 5 TAW-2000 microcomputer-controlled rock triaxial test equipment (a) Triaxial test equipment (b) Axial, circumferential and hydraulic measurement system

2.3 NMR T₂ analysis of granite specimens

Nuclear magnetic resonance (NMR) technology has been used in the field of rock mechanics to analyze the distribution and evolution of meso-pore structure inside the rock specimens. NMR technology is based on the principle of directional arrangement of fluid hydrogen atoms under the action of external magnetic field to measure the relaxation characteristics of fluid in the rock pores. The transverse relaxation time T_2 is composed of volume relaxation, surface relaxation and diffusion relaxation, which can be used to characterize the proportion of pores in the rock. The transverse relaxation time T_2 is:

$$\frac{1}{T_2} = \frac{1}{T_{2s}} + \frac{1}{T_{2v}} + \frac{1}{T_{2d}}$$

where: T_{2s} is surface relaxation time; T_{2v} is volume relaxation time; T_{2d} is diffusion relaxation time.

Because the transverse relaxation time is mainly controlled by surface relaxation, the latter two terms in the above formula can be ignored, that is, $T_2 = T_{2s}$. The above formula is simplified as:

$$\frac{1}{T_2} \approx \frac{1}{T_{2s}} = \rho_2 \frac{S}{V}$$

where: S is pore surface area (cm^2); V is pore volume (cm^3); ρ_2 is relaxation rate of rock surface (ms^{-1}).

The pore system of porous media can be regarded as composed of multiple independent diffusion units. Each diffusion unit has a specific pore surface area S_i and pore volume V_i , and each independent diffusion unit corresponds to a single relaxation time constant T_{2i} . Using CPMG sequence test, the total magnetization $M(t)$ of rock at time t can be expressed as:

$$M(t) = \sum \mathbf{M}_{0i} \exp\left(-\frac{t}{T_{2i}}\right)$$

Due to the continuity of rock pore size distribution, $M(t)$ can be expressed in the form of continuous integral:

$$\begin{aligned} M(t) &= \mathbf{M}_0 \int_0^\infty P(T_2) \exp\left(-\frac{t}{T_2}\right) dT_2 \\ &= \mathbf{M}_0 \int_0^\infty P(T_2) \exp\left(-\rho_2 \frac{S_i}{V_i} t\right) dT_2 \end{aligned}$$

where: $M_{0i}(0)$ is the magnetization vector of the i^{th} relaxation component at the initial time; $P(T_2)$ is the distribution density of T_2 .

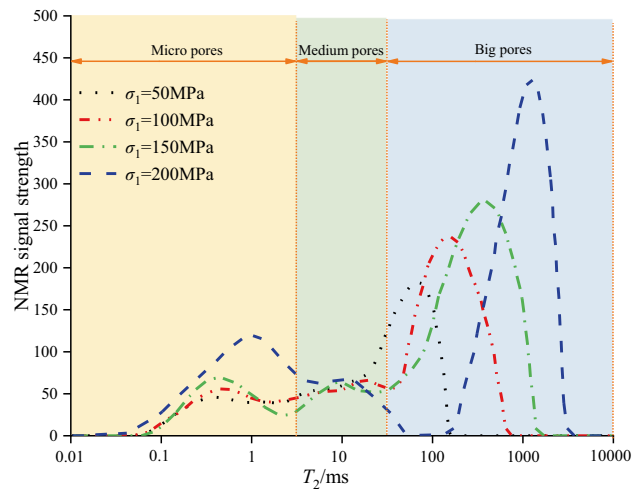


Fig.6 T_2 spectrum

It can be concluded that the T_2 spectrum distribution of NMR signal intensity reflects the size and distribution characteristics of pores in rock. The smaller the pore radius, the shorter the corresponding fluid relaxation time T_2 , and the more left on the T_2 spectrum distribution curve. The more fluid in a certain aperture range, the greater the nuclear magnetic signal intensity corresponding to T_2 value and the greater the peak value on T_2 spectrum curve.

The effect of external load has obvious influence on the distribution of pores in rock. Nuclear magnetic resonance technology can effectively characterize the effect of external load on the development of cracks in rock.

Figure 6 shows the variation of T_2 spectrum distribution of granite under different axial stress. According to the principle of rock NMR, the transverse relaxation time (T_2) is positively correlated with the pore size of the measured fluid. According to the relaxation characteristics of fluids in different pores, the pores of rock can be divided into three categories: the pores corresponding to $T_2 < 3$ ms are called micro pores, the pores corresponding to T_2 value in the range of 3~33 ms are called medium pores, and the pores corresponding to $T_2 > 33$ ms are called big pores.

Figure 6 shows the distribution of nuclear magnetic resonance T_2 spectrum of granite after different axial stress, the curve of σ_1 is 50 MPa has only two peaks, the other three T_2 curves have three peaks. It shows that the internal damage degree of granite increased significantly after the axial stress above 100 MPa, which is mainly manifested in the significant development of micro pores. The greater the axial stress, the more obvious the wave crest of the large crack moves to the right, indicating that the greater the stress, the faster the crack

expansion rate of granite and the more serious the rock damage. When the axial stress is 200 MPa, there is a discontinuity at the relaxation time of 100 for the T_2 curve, and the pore size of granite pore is no longer continuous. The expansion rate of micro pores is far lower than that of big pores. The proportion of the original medium pores developing into large crack is significantly larger than that of the micro pores expanding into medium pores.

With the increase of axial stress, the T_2 spectral area of granite increases gradually. It shows that the pore volume of rock increases with the increase of axial stress. The crest represents a big pore, and the area of the crest increases gradually. It shows that the big pores in the rock generally show an increasing trend, and the damage degree of the rock is further aggravated.

In the process of triaxial compression of granite, the fracture development of rock specimen is low and the expansion speed is slow under the condition of low axial stress, and it increases rapidly under the condition of high axial stress. In the low axial stress stage of triaxial compression of granite, the rock damage is mainly caused by the increase of the number of cracks. In the high axial stress condition, the rock damage is mainly caused by the number of cracks and the crack penetration.

3 Fracture propagation and mechanical properties of jointed rock mass specimens

3.1 Deformation characteristics of specimens with different joint dip angles

Figure 7 shows the stress–strain curves of rock mass specimens with non-penetrated joints with different joint dip

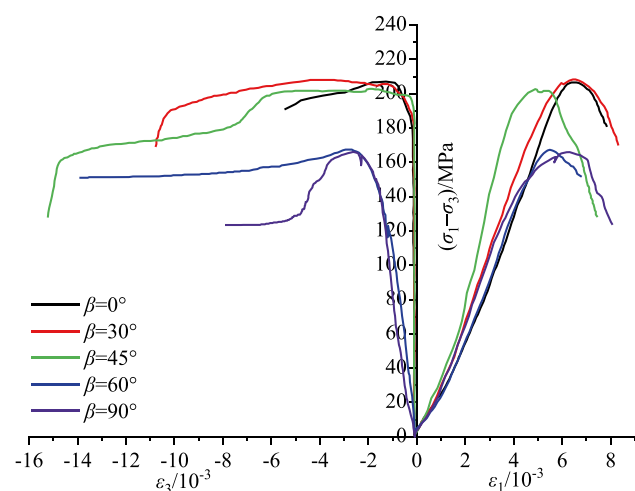


Fig. 7 Stress–strain curves of jointed rock mass specimens with different dip angles

angles when the water pressure is 2 MPa and the confining pressure is 5 MPa.

The stress–strain curves of rock mass specimens with non-penetrated joints with different joint dip angles can be seen that before reaching the peak stress, the specimens go through the compaction closure stage, linear elastic deformation stage, fracture stable expansion, and unstable expansion stage until the peak failure. The peak stress of the specimens decreases first and then increases with the increase of joint dip angle. The test results of five selected specimens with joint dip angles (0° , 30° , 45° , 60° , and 90°) show that the peak stress is the smallest when the joint dip angle is 60° . The peak stress of rock mass specimens with different joint dip angles increases with the increase of confining pressure, and its variation process is similar to that of intact rock specimens, but its characteristic stress is less than that of intact rock specimens.

The axial strain and circumferential strain of the specimen before and after the peak stress are roughly the same. When the confining pressure is 5 MPa, the circumferential strain of the specimen with a joint dip of 30° after the peak stress is more obvious. When the joint dip is 60° , the axial strain of the specimen reaching the peak stress point is the smallest.

Compared with the triaxial compression test results of the specimens, the confining pressure has an obvious restrictive effect on the stable and unstable crack propagation of the jointed rock mass specimens. When the jointed rock mass specimens reach the peak stress, the bearing capacity of the specimens decreases slowly under the confining pressure of 5 MPa, and the specimens show the characteristics of progressive failure.

When the confining pressure of specimens with different joint dip angles is 5 MPa, it can be seen from the stress–strain curve that the axial strain of rock specimens with different joint dip angles changes greatly after the peak. When the confining pressure is the same, the stress and strain of the specimens with different joint dip angles are different in each stage. When the confining pressure is 5 MPa, the axial strain beside the peak stress is relatively large when the joint dip angle is 30° , 45° , and 90° . The axial strain is relatively small when the joint dip angle is 0° and 60° , but the circumferential strain and volume stress of the jointed rock mass specimen are relatively small.

3.2 Mechanical characteristics of different specimens

The volumetric strain (ϵ_v) of rock specimen under triaxial compression is composed of elastic volumetric strain (ϵ_{ev}) and crack volumetric strain (ϵ_{cv}).

The volumetric strain formula is:

$$\epsilon_v = \epsilon_1 + 2\epsilon_3 \tag{6}$$

where axial strain ϵ_1 and lateral strain ϵ_3 are determined by experiment.

According to Hooke's theorem, the elastic volumetric strain (ϵ_{ev}) of rock specimen under conventional triaxial compression is:

$$\epsilon_{ev} = \frac{1-2\nu}{E}(\sigma_1 + 2\sigma_3) \tag{7}$$

where: E 、 ν are respectively the elastic modulus and Poisson's ratio of rock specimens in the linear elastic stage, σ_1 、 σ_3 are axial stress and lateral stress respectively. The crack volume strain (ϵ_{cv}) can be obtained by subtracting the elastic volume strain (ϵ_v) from the volume strain (ϵ_{ev}):

$$\epsilon_{cv} = \epsilon_v - \epsilon_{ev} = \epsilon_v - \frac{1-2\nu}{E}(\sigma_1 + 2\sigma_3) \tag{8}$$

In the linear elastic stage of rock, the internal peripheral cracks and defects do not expand and sprout. Therefore, the joint volume strain does not change with the increase of axial strain, and the joint volume strain axial strain curve is an approximate horizontal line segment. The end position of the horizontal section of the curve corresponds to the joint initiation strength point. After this point, the joint volume strain begins to expand, indicating that the rock deformation and failure enters stage III, and the joint begins to sprout and expand. After the rock failure deformation enters the unstable development stage, the macro-cracks begin to appear gradually. The volume gradually changes from compression to expansion, and the corresponding rock strength at the inflection point of volume strain axial strain curve is the damage strength value.

According to the rock mechanics test procedures, the curve of the elastic modulus of the specimen with the joint dip is obtained based on the rock stress–strain test results (Fig. 8).

The elastic modulus of jointed rock mass specimens is significantly smaller than that of intact specimens without joints, and the deformation parameters of specimens with different joint dip angles are also different. The elastic modulus of specimens with joint dip angles of 0°, 30°, and 90° is smaller, of which the elastic modulus of specimens with joint dip angles of 60° is the largest. The peak strength of specimens with joint dip angles of 60° is the lowest, and the bearing capacity can be achieved when the strain is relatively small load limit. The elastic modulus of specimens

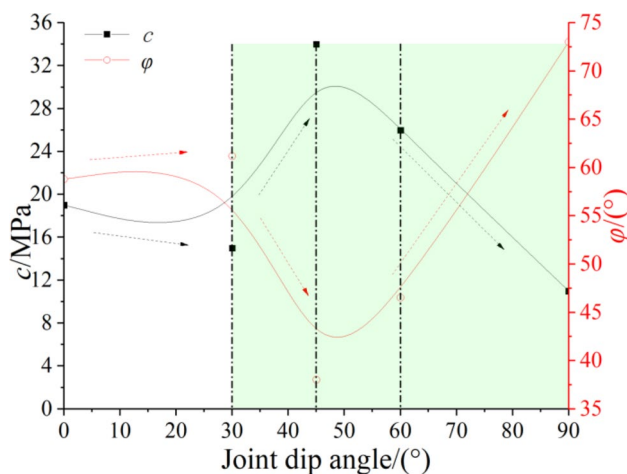


Fig. 9 Relationship between internal friction angle or cohesion and joint dip angle

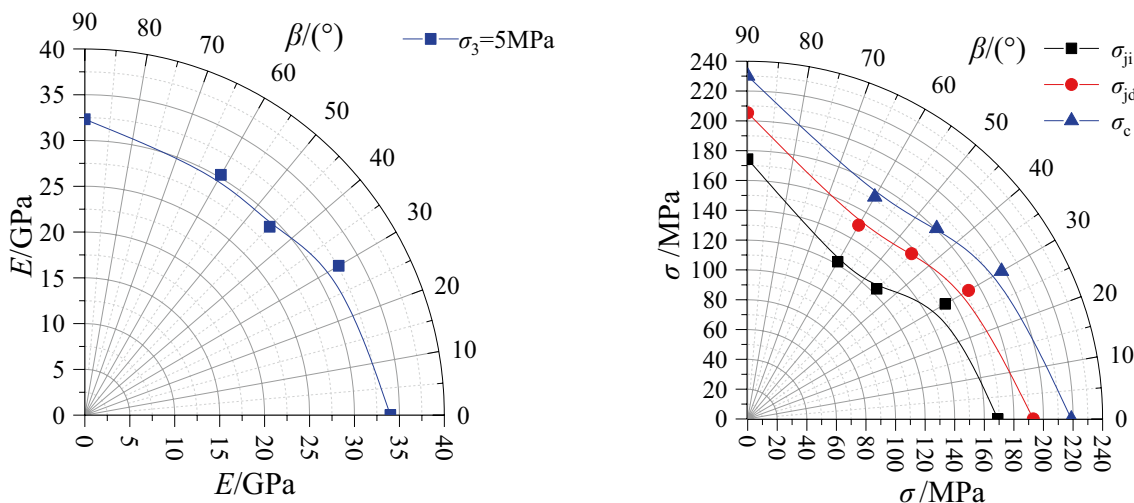


Fig. 8 Mechanical characteristics of different specimens with different joint dip

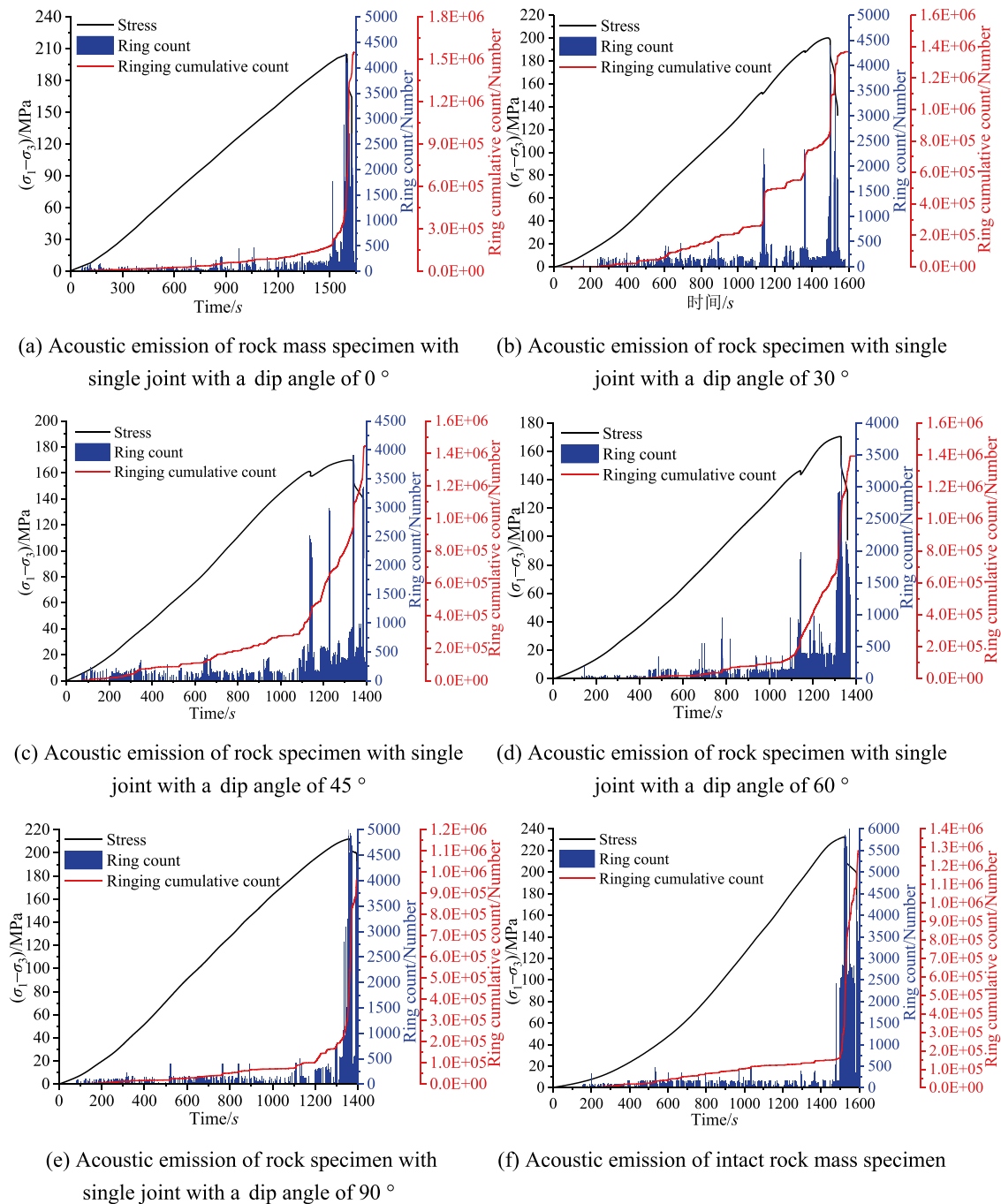


Fig. 10 Acoustic emission ring count and stress variation of rock mass specimen (a) Acoustic emission of rock mass specimen with single joint with a dip angle of 0° , (b) Acoustic emission of rock specimen with single joint with a dip angle of 30° , (c) Acoustic emission of

rock specimen with single joint with a dip angle of 45° , (d) Acoustic emission of rock specimen with single joint with a dip angle of 60° , (e) Acoustic emission of rock specimen with single joint with a dip angle of 90° , (f) Acoustic emission of intact rock mass specimen

with different joint dips increases gradually with the increase of confining pressure.

The specimen shows typical anisotropic characteristics and failure mechanisms. When the joint dip angle from 0° to 30° , the compressive strength of the specimen decreases slowly. When the joint dip angle is from 30° to 60° , the

compressive strength of the specimen decreases rapidly until the joint dip angle of 60° is the lowest. When the joint dip angle changes from 60° to 90° , the compressive strength of the specimens increases obviously, and the compressive

strength of the specimens with joint dip angles of 0° and 90° is the largest.

In each stage when the joint dip angle changes from 0°, 30°, 45° to 60°, the compressive strength of the specimens when the confining pressure is 5 MPa decreases by 1.46%, 15.57% and 0.65%. The variation curves of cohesion (c) and internal friction angle (φ) of the specimens with different joint dip angles are shown in Fig. 9.

With the increase of joint dip angle, the cohesion of the specimen shows an inverted U-shaped change, which increases first and then decreases. When the joint dip angle is 90°, the cohesion of the specimen reaches the minimum value of 11.05 MPa, reaches the maximum value of 34.12 MPa at 45°, and the minimum value is 32.37% between the maximum values. The internal friction angle of the specimen increases slightly and then decreases with the increase of joint dip angle. When the joint dip angle is 45°, the internal friction angle of the specimen reaches the minimum value of 73.02° and the maximum value of 38.03° at 90°, and the difference between the minimum value and the maximum value is 47.92%.

The analysis shows that the cohesion and internal friction angle of the specimen is greatly affected by the joint dip angle of the specimen because the failure stress and failure mode of the specimens with different joint dip angles are different, so the cohesion and internal friction angle of the specimen also has anisotropic characteristics.

3.3 Acoustic emission and failure characteristics of different specimens

Figure 10 shows the monitoring results of acoustic emission during triaxial compression failure of rock mass specimen with a single joint, in which the ring count is the ring generated when an event strikes the sensor. When the electrical signal formed by the ring exceeds the threshold, it can be counted as a ring count. As a comparison, the relationship between AE ring count and stress with the time of complete rock mass specimen is shown in Fig. 10 (f).

In the initial compaction stage of the specimen, the acoustic emission activity is weak, resulting in fewer

acoustic emission ringing counts, which corresponds to the closure of micro-cracks in the specimen. In the subsequent linear elastic deformation stage of the specimen, the acoustic emission events increase, the ring count increases, and changes in a small range. Currently, the specimen is mainly the initial damage evolution process. When the specimen enters the micro-crack, it germinates stably. In the expansion stage, the occurrence degree of acoustic emission events increases, and the ring count increases and changes in a relatively larger range.

When the unstable fracture propagation stage occurs in the specimen, the crack expands and penetrates, and the specimen begins to have large acoustic emission events. As shown in Figs. 10 (b), 10 (c), and 10 (d), the specimens with joint dip angles of 30°, 45°, and 60° have stress mutation points, and large acoustic emission events occur at the mutation points. The specimen with a joint dip angle of 30° has two sudden drops of stress and then continues to increase, accompanied by the rapid increase of acoustic emission ring count. As shown in Fig. 10 (c), when the joint dip angle is 45°, there is another active acoustic emission event between the first stress mutation point and the peak value, but there is no stress mutation, which indicates that the crack accumulation in the specimen will also lead to the instability of the specimen. As shown in Fig. 10 (d), the specimen with a joint dip angle of 60° also has an approximate phenomenon before the first stress mutation point.

When the specimen reaches the peak strength, the acoustic emission activity of the specimen is extremely active. When the stress of the specimen reaches the post-peak strength, the number of acoustic emission events begins to decrease rapidly, and the ringing count reaches the maximum at the peak point of the specimen. The crack penetration rate in the specimen increases and the bearing capacity of the specimen begins to decrease rapidly. In the post-peak stage, under the action of the residual strength of the specimen, the crack of the specimen continues to expand and the bearing capacity of the specimen increases. The load fluctuates and decreases, and the acoustic emission ringing count also changes with the change of stress.

Table 1 Parameters of CPMG sequence

| System parameter type | Parameter value | System parameter type | Parameter value |
|--|-----------------|---------------------------------------|-----------------|
| System magnetic field strength/T | 0.52 | Sampling points | 94,900 |
| RF signal center frequency/MHz | 12 | Waiting time for repeated sampling/ms | 2000 |
| RF signal center frequency | 679,368.4 | Analog gain | 5.0 |
| Offset of RF signal frequency/Hz | | | |
| RF 90° pulse width-P1/ μ s | 4.2 | Data radius | 1 |
| RF 180° pulse width-P2/ μ s | 9.6 | Stacking times | 8 |
| Control parameters of sampling starting point/ms | 0.020 | Number of echoes | 5000 |

There is a strong correlation between the acoustic emission ring count and the peak strength of jointed rock mass specimens. As shown in Fig. 10 (d), the peak strength of specimens with a joint dip angle of 60° is the lowest, and the acoustic emission ring count is also less than that of specimens with a joint dip angle of other angles. There is a corresponding relationship between AE ringing count and stress of specimens with different joint dip angles, and the number of AE events can better reflect the stress characteristic points of specimens.

It can be seen from Fig. 10 (f) that there is no bimodal or multimodal phenomenon in the stress time curve of the complete rock mass specimen. Although the acoustic emission data collected in the test has certain volatility, the active acoustic emission phenomenon does not appear until the specimen approaches the peak stage until specimen is damaged. The acoustic emission activity remains relatively active.

3.4 Failure modes of jointed rock mass specimens

Representative jointed rock mass specimens are selected for failure mode analysis. By comparing the morphology of main cracks and secondary cracks of rock mass specimens with different joint dip angles, the failure modes and mechanisms are analyzed. As shown in Table 1, red represents the main cracks and blue represents the secondary cracks, gray indicates local block falling or about to fall.

According to the above failure characteristics of the specimens, the failure forms of the specimens can be divided into tension failure, composite tension shear failure, and shear failure along the joint direction (Fig. 11).

The main cracks of jointed rock mass specimen are mainly the cracks that originate at the joint tip and expand along the axial direction of the specimen until the specimen loses its bearing capacity. The secondary cracks have a certain correlation with the joint dip angle. When the joint dip angle is small, the secondary cracks of jointed rock mass specimens expand axially at the joint tip, and when the joint dip angle is small. When the dip angle is large, the secondary cracks roughly expand radially.

For the rock mass specimen with single joints, the independent falling off the block is mainly near the tip of the joint, while the independent falling off block of rock mass specimen is mainly on the inner side of the joint, which represents the weakening area of mechanical properties of the specimen caused by the crack initiation and expansion process of the rock mass specimen with joints.

The seepage pressure plays a positive role in the process of rock fracture and failure. The seepage pressure in the crack reduces the normal stress on the crack surface and increases the effective shear driving force on the crack surface.

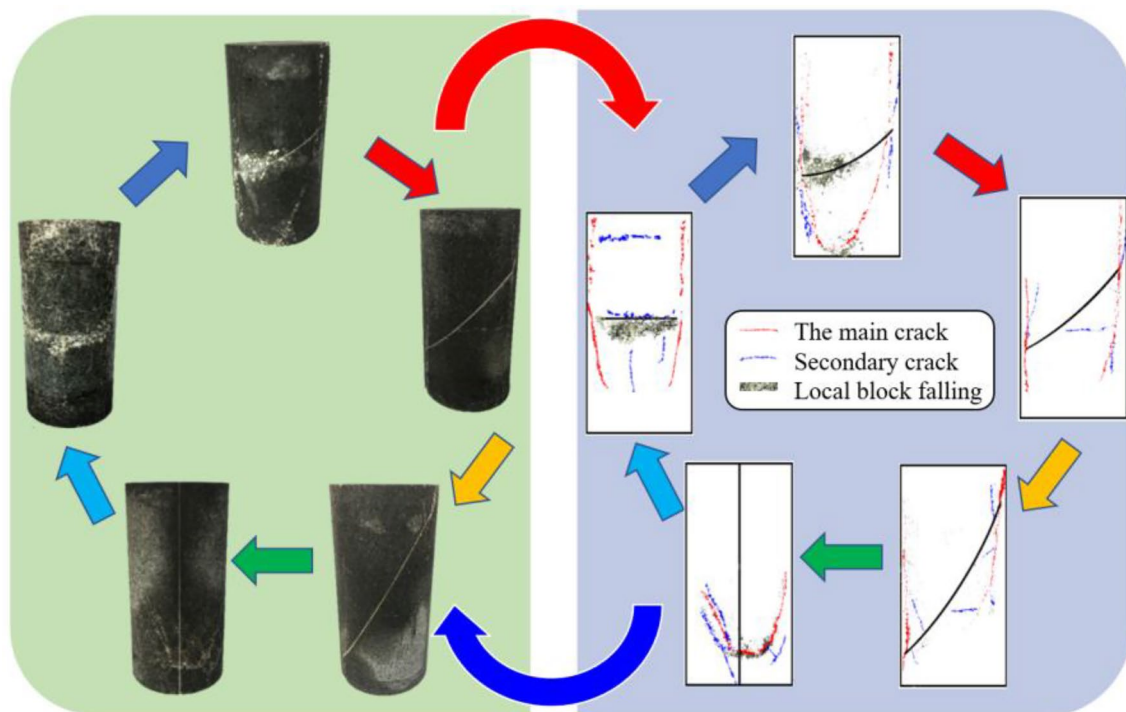


Fig. 11 Failure modes of jointed rock mass specimens

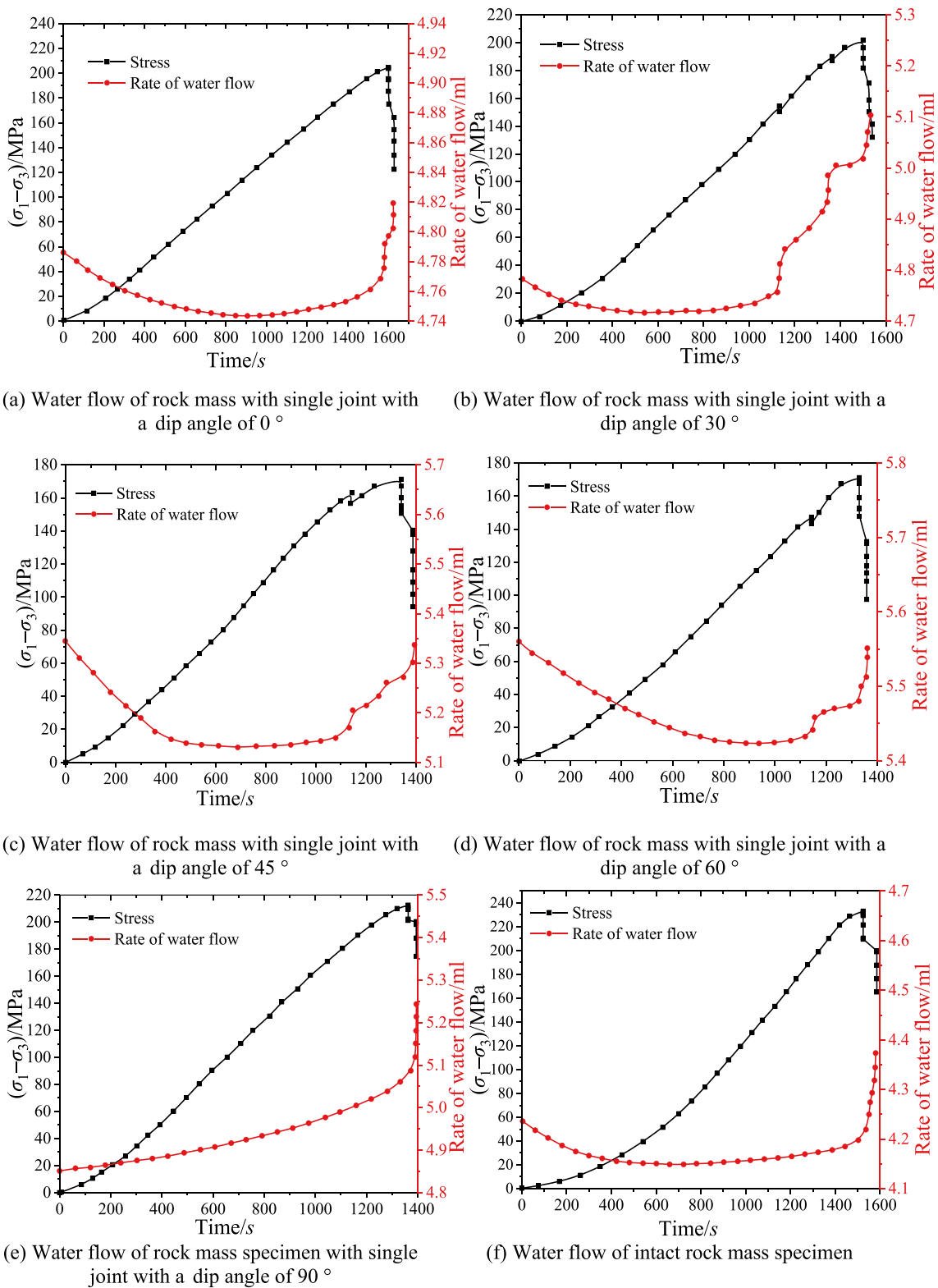


Fig. 12 Variation of stress and water flow of rock mass specimen with time, (a) Water flow of rock mass with single joint with a dip angle of 0° , (b) Water flow of rock mass with single joint with a dip angle of 30° , (c) Water flow of rock mass with single joint with a dip

angle of 45° , (d) Water flow of rock mass with single joint with a dip angle of 60° , (e) Water flow of rock mass specimen with single joint with a dip angle of 90° , (f) Water flow of intact rock mass specimen

4 Evolution mechanism of permeability with different dip angle

4.1 Water flow variation and water pressure deterioration

Rock pores and primary micro-fracture structure are used as the seepage path of fluid flow, the opening and closing of seepage throat channel determine the permeability of bedding rock.

Under the action of osmotic pressure (p_w), the effective confining pressure of rock specimen can be regarded as:

$$\sigma_{3\text{eff}} = \sigma_3 - p_w \quad (9)$$

where $\sigma_{3\text{eff}}$ is the effective confining pressure, σ_3 is confining pressure.

When the water pressure is 2 MPa and the confining pressure is 5 MPa, the relationship between water flow, stress, and time during triaxial compression failure of the specimen is shown in Fig. 12. The specimens were selected as jointed rock mass specimens with different dip angles and intact rock specimens for comparative analysis.

The water flow curves of the jointed rock mass specimens with different dip angles (except for the specimen with a joint dip angle of 90°) and the intact specimens show the trend that the water flow decreases first and then increases with time. In the initial compaction stage of the specimen, under the combined action of confining pressure and axial pressure, it is more difficult for water to pass through the relatively dense rock specimen, and only part of the water flows to the upper part of the specimen through the outer wall and joints. The flow rate decreases, and the water flow rate shows an increasing trend when cracks appear in the specimen. When the water flow increases rapidly, the stress of the specimen decreases suddenly. When the specimen reaches the peak stress, the water flow increases at the maximum speed until the specimen is destroyed.

Because the intact rock specimen has no prefabricated joints, the water flow channel is mainly the outer wall of the specimen before the specimen is damaged, and the water flow is the smallest. Until the specimen produces macro-cracks, the water flow channel increases rapidly, and the water flow increases rapidly, but the water flow is still significantly less than that of the jointed rock mass specimen. The water flow of jointed rock mass specimens begins to increase before reaching the peak stress, and only the water flow of intact rock specimens remains unchanged before the peak stress, indicating that the water enters the prefabricated joints under the action of water pressure and confining pressure during triaxial loading, and plays a role in the deterioration of water pressure on the joints.

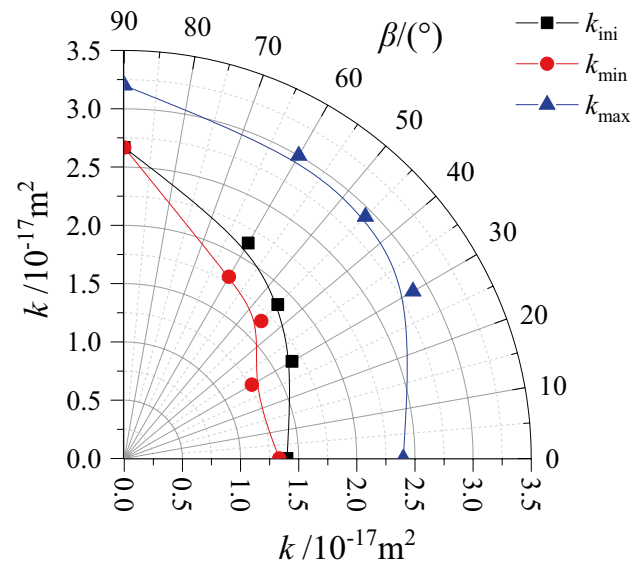


Fig. 13 Relationship curve between permeability and joint dip angle of jointed rock mass specimens

4.2 Permeability variation of specimens with different joint dip angles

Permeability is an average permeability coefficient property of rock mass media, and it can be calculated by the following formula:

$$k = \frac{q\mu L}{A\Delta p} \quad (10)$$

where k is the permeability of fracture specimen, m^2 ; q is the flow in the seepage process, $\text{m}^3 \cdot \text{s}^{-1}$; μ is the viscosity coefficient, $\text{Pa} \cdot \text{s}$; L is the crack length, m ; $A = a \cdot b$ is the seepage cross-sectional area, m^2 , a is the crack width, m ; b is the width of fracture section, m ; Δp is the seepage pressure difference, MPa .

Permeability is the inherent property of rock mass. The initial permeability of the specimens can be obtained by calculating the seepage flow before the initial loading and substituting the flow into Darcy formula. Figure 13 shows the relationship between rock initial permeability and joint dip angle. It can be concluded that the initial permeability increased significantly with the increase of joint dip angle. In the process of joint dip angle from 0 to 30° , 30° to 45° , 45° to 60° and 60° to 90° , the average increase of initial permeability of rock mass specimens is $0.27 \times 10^{-17} \text{m}^2$, $0.2 \times 10^{-17} \text{m}^2$, $0.27 \times 10^{-17} \text{m}^2$ and $0.53 \times 10^{-17} \text{m}^2$ respectively.

Figure 13 shows the variation curve of minimum permeability and maximum permeability with joint dip angle. In

the process of joint dip angle from 0 to 30°, 30° to 45°, 45° to 60° and 60° to 90°, the average increase of minimum permeability of rock mass specimens is $-0.07 \times 10^{-17} \text{m}^2$, $0.4 \times 10^{-17} \text{m}^2$, $0.13 \times 10^{-17} \text{m}^2$ and $0.86 \times 10^{-17} \text{m}^2$ respectively. This shows that the increase rate of k_{\min} shows a "V" change trend with the increase of joint dip angle, and the maximum increase rate is obtained between 60° and 90°. In the process of joint dip angle from 0 to 30°, 30° to 45°, 45° to 60° and 60° to 90°, the average increase of maximum permeability of rock mass specimens is $0.47 \times 10^{-17} \text{m}^2$, $0.07 \times 10^{-17} \text{m}^2$, $0.07 \times 10^{-17} \text{m}^2$ and $0.2 \times 10^{-17} \text{m}^2$ respectively. This shows that with the increase of joint dip angle, the increase rate of k_{\max} shows a gradual change trend, and the maximum increase rate is obtained between 0° and 30°.

4.3 Evolution law of permeability coefficient of jointed rock mass specimens

The rock permeability coefficient refers to the hydraulic conductivity coefficient, which indicates the difficulty of fluid passing through the porous structure. It can be obtained by formula:

$$K = \frac{k \cdot \gamma}{\mu} = \frac{qL\gamma}{A\Delta p} \quad (11)$$

where K is permeability coefficient, $\text{m} \cdot \text{s}^{-1}$; γ is unit weight; μ is fluid viscosity, Pa·s.

Through calculation, the evolution law of permeability coefficient of jointed rock mass specimens with different joint dip angles, the evolution law of permeability coefficient of jointed rock mass specimens under different confining pressure are obtained. The permeability coefficient of jointed rock mass specimens with different joint dip angles is selected under confining pressure of 5 MPa. The variation

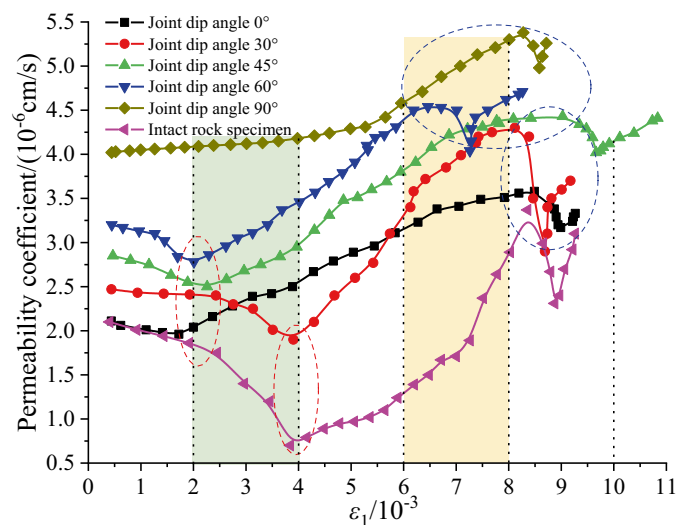
curve of permeability coefficient when the water pressure is 2 MPa is shown in Fig. 14.

It can be seen from Fig. 14 that the initial permeability coefficient of jointed rock mass specimen decreases with the increase of confining pressure, which is because the increase of confining pressure will limit the flow of water. With the increase of strain, the axial strain and radial strain of the specimen under the action of axial stress increase gradually, and the restriction of fluid flow increases gradually, so the permeability coefficient of the specimen decreases gradually. When the specimen generates micro-cracks at the joint tip under the action of axial pressure and evolves and expands with the increase of pressure, the channel of fluid flow gradually increases, and the permeability coefficient of the specimen gradually increases. When the specimen reaches the peak value, a through crack is generated in the specimen, which provides a through water channel for fluid flow. Therefore, the permeability coefficient of the specimen increases the peak value.

However, when the specimen enters the post-peak stage, due to the residual stress and strain softening of the specimen, the internal structure of the specimen is dislocated, affecting the fluid flow, and the permeability coefficient of the specimen decreases. However, when the specimen continues to fail under pressure, the macro-crack of the specimen appears the phenomenon of compaction and closure, and the permeability coefficient of the specimen will continue to increase.

However, there are some differences in the changes of specimens with a joint dip angle of 90° in the initial stage. This is because the specimens with a joint dip angle of 90° always have water diversion channels from top to bottom, and are less affected by confining pressure and pressure. The permeability coefficient of the specimens increases gradually only with the initiation, evolution, and expansion of cracks.

Fig. 14 Evolution law of permeability coefficient of jointed rock mass specimens



The influence process and mechanism of joint dip angle on the evolution of permeability are complex, which are not only affected by the water-conducting structure of different joint dip angles and the characteristics of crack propagation, but also affected by the joint's shear expansion, shear contraction and the wear of the bulge.

The initial permeability coefficient of the intact rock specimen is the smallest, and the initial permeability coefficient of the jointed rock mass specimen increases gradually with the increase of the joint dip angle.

5 Conclusion

Based on the analysis of joint occurrence and mineral composition of surrounding rock, the experimental study on NMR T_2 characteristic law and permeability evolution mechanism is carried out. The changes of mechanical properties, acoustic emission, and permeability characteristics of rock specimens with different joint dip angles are studied. Combined with microstructure and joint tip propagation mechanism, fracture propagation and permeability evolution mechanism of rock specimens with different joint dip angles are revealed, and the following conclusions can be drawn:

- (1) The crack propagation law of rock samples is analyzed by NMR test. The greater the axial stress, the more obvious the wave crest of the large crack moves to the right, indicating that the greater the stress, the faster the crack expansion rate of granite and the more serious the rock damage. The characteristic law of rock NMR T_2 spectrum curve under hydraulic coupling is very significant. The proportion of the original medium pores developing into large crack is significantly larger than that of the micro pores expanding into medium pores.
- (2) The peak stress of the specimens decreases first and then increases with the increase of joint dip angle. The cohesion of the specimen first increases and then decreases, and the inverted U-shaped change and the internal friction angle of the specimen show a change trend of small increase and then decrease. The results show that the mechanical properties of rock specimens are influenced with joint dip angle, which have anisotropic characteristics. In the low axial stress stage of triaxial compression of granite, the rock damage is mainly caused by the increase of the number of cracks. In the high axial stress condition, the rock damage is mainly caused by the number of cracks and the crack penetration.
- (3) The development law of acoustic emission events of jointed rock mass specimens is experimentally studied, the correlation between acoustic emission ring count and peak stress of specimens is obtained, and the initial damage evolution process is analyzed. Combined with the analysis of failure modes of rock specimens with different joint dip angles, the damage evolution mechanism and crack propagation law of specimens are studied. The main cracks of jointed rock mass specimens are mainly the cracks that originate from the joint tip and extend along the axial direction of the specimen until the specimen loses its bearing capacity. The secondary cracks have a certain correlation with the joint dip angle.
- (4) Through the permeability test of jointed rock specimens, the variation relationship between permeability and effective stress is analyzed, and the permeability evolution law of rock samples with different joint dip angles is obtained. With the increase of strain, the axial strain of the specimen under the action of axial stress gradually increases, the permeability coefficient of the specimen gradually decreases. When the specimen is under axial pressure, micro-cracks are generated at the joint tip and evolve and expand with the increase of pressure. The channel of fluid flow gradually increases and the permeability coefficient of the specimen gradually increases.
- (5) The seepage pressure plays a positive role in the process of rock fracture and failure. The seepage pressure in the crack reduces the normal stress on the crack surface and increases the effective shear driving force on the crack surface. During the whole stress–strain process of continuous loading under hydro-mechanical coupling, the permeability decreases gradually with the increase of axial strain. After the elastoplastic stage, the change trend of permeability is determined by the two main factors (the initiation and expansion of rock micro-cracks, the crushing of rock skeleton particles). The initiation and expansion of rock micro-cracks play a positive role in the increase of permeability, while the compression zone formed by the crushing of rock skeleton particles inhibits the increase of permeability.

Acknowledgements This work is supported by China Postdoctoral Science Foundation (Grant No. 2021M701540).

Declarations

Conflict of interest The authors declare that they have no known competing financial interests or personal relationships that could have appeared to influence the work reported in this paper.

Data availability The data that support the findings of this study are available from the first and corresponding authors on reasonable request.

References

- Ardeshir A, Amiri M, Ghasemi Y et al (2014) Risk assessment of construction projects for water conveyance tunnels using fuzzy fault tree analysis. *Inter J Civil Eng* 12(4):396–412
- Cai M (2016) Prediction and prevention of rockburst in metal mines—A case study of Sanshandao gold mine. *J Rock Mech Geotech Eng* 8(2):204–211
- Castro R, Trueman R, Halim A (2007) A study of isolated draw zones in block caving mines by means of a large 3D physical model. *Int J Rock Mech Min Sci* 44(6):860–870
- Cui G, Wei J, Feng XT et al (2019) Preliminary study on the feasibility of co-exploitation of coal and uranium. *Int J Rock Mech Min Sci* 123:104098
- Gao R, Yan H, Ju F et al (2018) Influential factors and control of water inrush in a coal seam as the main aquifer. *Int J Min Sci Technol* 28(2):187–193
- Golian M, Teshnizi ES, Nakhaei M (2018) Prediction of water inflow to mechanized tunnels during tunnel-boring-machine advance using numerical simulation. *Hydrogeol J* 26(8):2827–2851
- Hassani H, Hloušek F, Alexandrakos C et al (2018) Migration-based microseismic event location in the Schlema-Alberoda mining area. *Int J Rock Mech Min Sci* 110:161–167
- Khavé GJ (2014) Delineating subterranean water conduits using hydraulic testing and machine performance parameters in TBM tunnel post-grouting. *Int J Rock Mech Min Sci* 70:308–317
- LaMoreaux JW, Wu Q et al (2014) New development in theory and practice in mine water control in China. *Carbon Evap* 29(2):141–145
- Lee H, Lee JW et al (2021) Permeability evaluation for artificial single rock fracture according to geometric aperture variation using electrical resistivity. *J Rock Mech Geotech Eng* 13(4):787–797
- Li S, Liu R, Zhang Q et al (2016) Protection against water or mud inrush in tunnels by grouting: a review. *J Rock Mech Geotech Eng* 8(5):753–766
- Li G, Meng Z, Wang X et al (2017) Hydrochemical prediction of mine water inrush at the Xinli Mine. *China Mine Water Environ* 36(1):78–86
- Liu Z, Dang W, He X (2012) Undersea safety mining of the large gold deposit in Xinli District of Sanshandao Gold Mine. *Int J Miner Metall Mater* 19(7):574–583
- Ma D, Rezaia M, Yu HS et al (2017) Variations of hydraulic properties of granular sandstones during water inrush: effect of small particle migration. *Eng Geol* 217:61–70
- Małachowski K (2018) The biggest surface mining disaster in Poland and its economic results. *Eur J Service Manag* 28(4/2):247–255
- Pappalardo G (2018) First results of infrared thermography applied to the evaluation of hydraulic conductivity in rock masses. *Hydrogeol J* 26(2):417–428
- Polak K, Rózkowski K, Czaja P (2016) Causes and effects of uncontrolled water inrush into a decommissioned mine shaft. *Mine Water Environ* 35(2):128–135
- Ren C, Li B, Xu J et al (2020) A novel damage-based permeability model for coal in the compaction and fracturing process under different temperature conditions. *Rock Mech Rock Eng* 53(12):5697–5713
- Shi L, Wang Y, Qiu M et al (2019) Assessment of water inrush risk based on the groundwater modeling system—a case study in the Jiaojia Gold Mine Area. *China Arabian J Geosci* 12(24):1–17
- Song W, Liang Z (2021) Theoretical and numerical investigations on mining-induced fault activation and groundwater outburst of coal seam floor. *Bull Eng Geol Env* 80(7):5757–5758
- Vaziri V, Khademi Hamidi J, Sayadi AR (2018) An integrated GIS-based approach for geohazards risk assessment in coal mines. *Enviro Earth Sci* 77(1):1–18
- Wang SF, Li XB, Wang DM (2016) Mining-induced void distribution and application in the hydro-thermal investigation and control of an underground coal fire: A case study. *Process Saf Environ Prot* 102:734–756
- Wang S, Li X, Wang S (2017) Separation and fracturing in overlying strata disturbed by longwall mining in a mineral deposit seam. *Eng Geol* 226:257–266
- Wang SF, Li XB, Yao JR et al (2019) Experimental investigation of rock breakage by a conical pick and its application to non-explosive mechanized mining in deep hard rock. *Int J Rock Mech Min Sci* 12:104063
- Wang J, Zhang Y, Qin Z et al (2020) Analysis method of water inrush for tunnels with damaged water-resisting rock mass based on finite element method-smooth particle hydrodynamics coupling. *Comput Geotech* 126:103725
- Wolkersdorfer C, Nordstrom DK, Beckie RD et al (2020) Guidance for the integrated use of hydrological, geochemical, and isotopic tools in mining operations. *Mine Water Environ* 39(2):204–228
- Wu J, Xu S, Zhou R et al (2016) Scenario analysis of mine water inrush hazard using Bayesian networks. *Saf Sci* 89:231–239
- Wu N, Liang Z, Li Y et al (2019) Stress-dependent anisotropy index of strength and deformability of jointed rock mass: insights from a numerical study. *Bull Eng Geol Env* 78(8):5905–5917
- Xue Y, Kong F, Qiu D et al (2020) The classifications of water and mud/rock inrush hazard: a review and update. *Bull Eng Geol Env* 11(2):221–321
- Yan B, Guo Q, Ren F et al (2020a) Modified Nishihara model and experimental verification of deep rock mass under the water-rock interaction. *Int J Rock Mech Min Sci* 128:104250
- Yan B, Ren F, Cai M et al (2020b) Bayesian model based on Markov chain Monte Carlo for identifying mine water sources in Submarine Gold Mining. *J Clean Prod* 253:120008
- Yao B, Bai H, Zhang B (2012) Numerical simulation on the risk of roof water inrush in Wuyang Coal Mine. *Int J Min Sci Technol* 22(2):273–277
- Yu J, Li H, Chen X (2013) Triaxial experimental study of associated permeability-deformation of sandstone under hydro-mechanical coupling. *Chin J Rock Mech Eng* 32(6):1203–1213
- Zhang HQ, He YN, Tang CA et al (2009) Application of an improved flow-stress-damage model to the criticality assessment of water inrush in a mine: a case study. *Rock Mech Rock Eng* 42(6):911
- Zhang SG, Liu JQ, Chen PP (2015) Experimental research on mechanical properties of granite under water-rock coupling. *Chin J Rock Mech Eng* 34(3):520–527
- Zhou Q, Herrera J, Hidalgo A (2018) The numerical analysis of fault-induced mine water inrush using the extended finite element method and fracture mechanics. *Mine Water Environ* 37(1):185–195

Publisher's Note Springer Nature remains neutral with regard to jurisdictional claims in published maps and institutional affiliations.

Springer Nature or its licensor (e.g. a society or other partner) holds exclusive rights to this article under a publishing agreement with the author(s) or other rightsholder(s); author self-archiving of the accepted manuscript version of this article is solely governed by the terms of such publishing agreement and applicable law.